

RESEARCH ARTICLE

10.1002/2016JB013045

Key Points:

- Gravity-driven deformation of the dome occurs in association with large-magnitude, low-frequency earthquakes
- The deformation is recorded as a localized, high-frequency tremor-like seismic signal
- Extraction of 3-D surface displacement fields reveal partition of motion along clearly defined internal dome structures

Supporting Information:

- Supporting Information S1

Correspondence to:

J. T. Salzer,
salzer@gfz-potsdam.de

Citation:

Salzer, J. T., W. A. Thelen, M. R. James, T. R. Walter, S. Moran, and R. Denlinger (2016), Volcano dome dynamics at Mount St. Helens: Deformation and intermittent subsidence monitored by seismicity and camera imagery pixel offsets, *J. Geophys. Res. Solid Earth*, 121, 7882–7902, doi:10.1002/2016JB013045.

Received 1 APR 2016

Accepted 2 OCT 2016

Accepted article online 5 OCT 2016

Published online 14 NOV 2016

Volcano dome dynamics at Mount St. Helens: Deformation and intermittent subsidence monitored by seismicity and camera imagery pixel offsets

Jacqueline T. Salzer¹, Weston A. Thelen^{2,3}, Mike R. James⁴, Thomas R. Walter¹, Seth Moran³, and Roger Denlinger³

¹Department 2: Physics of the Earth, GFZ German Research Centre for Geosciences, Potsdam, Germany, ²Hawaiian Volcano Observatory, U.S. Geological Survey, Hawai'i Volcanoes National Park, Hawaii, USA, ³Cascades Volcano Observatory, U.S. Geological Survey, Vancouver, Washington, USA, ⁴Lancaster Environment Centre, Lancaster University, Lancaster, UK

Abstract The surface deformation field measured at volcanic domes provides insights into the effects of magmatic processes, gravity- and gas-driven processes, and the development and distribution of internal dome structures. Here we study short-term dome deformation associated with earthquakes at Mount St. Helens, recorded by a permanent optical camera and seismic monitoring network. We use Digital Image Correlation (DIC) to compute the displacement field between successive images and compare the results to the occurrence and characteristics of seismic events during a 6 week period of dome growth in 2006. The results reveal that dome growth at Mount St. Helens was repeatedly interrupted by short-term meter-scale downward displacements at the dome surface, which were associated in time with low-frequency, large-magnitude seismic events followed by a tremor-like signal. The tremor was only recorded by the seismic stations closest to the dome. We find a correlation between the magnitudes of the camera-derived displacements and the spectral amplitudes of the associated tremor. We use the DIC results from two cameras and a high-resolution topographic model to derive full 3-D displacement maps, which reveals internal dome structures and the effect of the seismic activity on daily surface velocities. We postulate that the tremor is recording the gravity-driven response of the upper dome due to mechanical collapse or depressurization and fault-controlled slumping. Our results highlight the different scales and structural expressions during growth and disintegration of lava domes and the relationships between seismic and deformation signals.

1. Introduction

1.1. Overview

Andesitic and dacitic lava domes are viscous bodies of lava extruded in the summit region or the flank of a volcano over periods of days to decades. Structural instabilities and resulting collapses can lead to far-reaching debris avalanches and pyroclastic flows [Voight, 2000] and pose a significant hazard for the surrounding population.

The internal structure of a lava dome also has a strong impact on the eruptive process. In particular, the development of shear bands and their propagation into the dome is a key process controlling transitions between endogenous and exogenous styles of dome growth [Hale and Wadge, 2008]. Substantial morphological and structural changes may also be strongly dependent on the parameters governing the eruption, such as variations in the supply rate and magma rheology [Husain et al., 2014].

Deformation monitoring at dome-building volcanoes may allow resolving the presence of long-term internal dome structures [Beauducel et al., 2006; James and Varley, 2012; Salzer et al., 2014] which are critical for numerical modeling [Hale et al., 2009]. However, these signals are mixed with many other processes associated with dome growth that may lead to deformation over a wide range of temporal and spatial scales. For example, internal pressurization of the lava dome may have large effects on the development of an eruption [Sparks, 1997] but may also lead to deformation due to the repeated sealing of gas pathways on timescales of minutes [Johnson et al., 2014] to days or weeks [Ichihara et al., 2013; Matthews et al., 1997]. Experimental data

show that on timescales of hours to years dome deformation may also be driven by densification due to the viscous reorganization of pores by surface tension [Kennedy *et al.*, 2016].

Data sampling at high temporal resolution has also revealed possible links between seismic signals and mass movement at volcanic domes, e.g., related to inflation-deflation cycles produced by repeated conduit pressurization at Montserrat [Voight *et al.*, 1999]. Long-period events at the Santiaguito dome can be attributed in time and magnitude to brittle failure of the carapace due to degassing events [Johnson *et al.*, 2008]. A connection between thermal exhalations, seismic events and dome surface displacements has also been observed at the dome of Volcan de Colima while extruding over the crater rim [Walter *et al.*, 2013a]. Combining the analysis of seismic and deformation data is therefore essential for improving our understanding of the processes controlling them. However, quantifying deformation at volcanic domes and comparison between different events over longer time spans is often challenging due to difficult access, the lack of continuously operating systems, and the small magnitude of the deformation. In this work, we analyze an existing data set using novel techniques in order to evaluate dome deformation associated with earthquakes at Mount St. Helens between June and August 2006.

1.2. The 2004–2008 Eruption of Mount St. Helens

During the 2004–2008 dome-building eruption of Mount St. Helens, extrusion of a series of dacite spines as well as endogenous growth constructed a dome complex at the base of the crater floor, south of the preexisting dome from the 1980s [Vallance *et al.*, 2008]. An optical camera monitoring system was installed on the surrounding crater rim by the USGS Cascades Volcano Observatory (CVO), allowing the observation of the growing dome from multiple perspectives. The collected data set has successfully been used to determine variations in the extrusion rate and evaluate the morphological evolution of the dome complex throughout the eruption [Major *et al.*, 2008, 2009]. The internal dome structure was marked by discontinuities created by spine formation and also by faulting at the conduit margin and within the spines [Cashman *et al.*, 2008].

On timescales of months to years, the extrusion rate at Mount St. Helens showed a quasi-exponential decrease over the course of the eruption [Mastin *et al.*, 2009; Diefenbach *et al.*, 2012] before ceasing in January 2008 [Dzurisin *et al.*, 2015]. Previous studies revealed variations in the extrusion velocities observed at the dome over sequences of daily camera images from July 2006 [Walter, 2011]. However, the mechanism behind these fluctuations and their relationship to seismic data remained to be studied.

Over prolonged periods, the seismic data were marked by shallow, often regular and repetitive small long-period (LP) earthquakes, also called “drumbeats” due to their repetitive behavior. Occasionally, larger $M > 1$ earthquakes were also recorded, as well as higher-frequency volcano-tectonic earthquakes and volcanic tremor [Moran *et al.*, 2008b; Thelen *et al.*, 2008]. The rate of the larger earthquakes varied but were recorded between three and seven times per day in the summer months of 2006.

The larger events and the drumbeats shared some similarities in source depth, seismic frequencies, and the characteristics of the associated infrasound signals [Matoza *et al.*, 2009; Moran *et al.*, 2008b]. This may suggest a common source mechanism for the smaller LP earthquakes and the larger events, with the main difference being only the event magnitude. Thus, the models proposed for the generation of the drumbeat seismicity have also been applied to the larger earthquakes at Mount St. Helens [Kendrick *et al.*, 2012; Waite *et al.*, 2008].

The mechanisms that have been suggested as possible sources for the drumbeat seismicity and the larger earthquakes at Mount St. Helens fall into two main categories [Chouet and Matoza, 2013]: on the one hand, brittle fracture and stick-slip behavior controlled by friction at the conduit wall [Iverson *et al.*, 2006; Kendrick *et al.*, 2012, 2014] and, on the other hand, interactions with the hydrothermal system, resulting in the repeated sealing and pressurization of a steam-filled crack beneath the crater floor [Waite *et al.*, 2008; Matoza *et al.*, 2009, 2015].

The possible association of seismicity with stick-slip and episodic changes in the extrusion behavior of the plug as suggested by Iverson *et al.* [2006] led to various attempts to measure short-term deformation at Mount St. Helens, including the installation of a tiltmeter network [Anderson *et al.*, 2010] and a high-resolution camera aimed at capturing exclusively the motion of features on the exhumed conduit fault. Deformation associated with the earthquakes could not be identified in the camera data; however, some of the larger events showed permanent offsets in the tiltmeters [Anderson *et al.*, 2010].

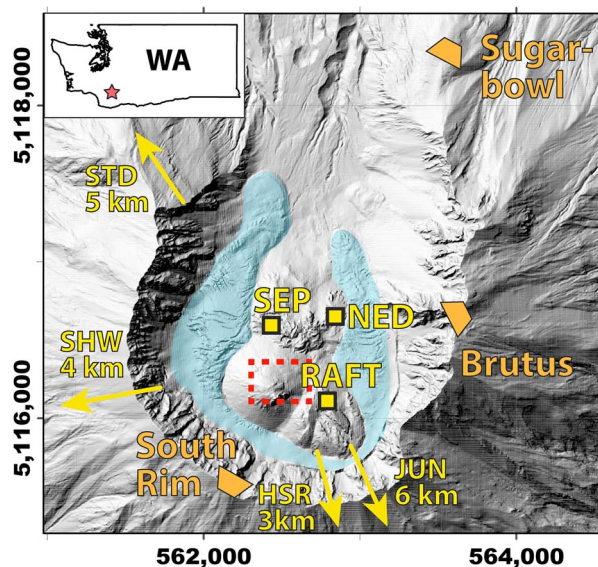


Figure 1. Shaded relief map of the Mount St. Helens summit, based on the USGS National Elevation Dataset (2004) and the 18 August 2006 DEM from Messerich *et al.* [2008]. Locations of the cameras (Sugarbowl, Brutus, and South Rim) are shown in orange and the seismometers (SEP, NED and RAFT) in yellow. The seismic stations HSR, JUN, SHW and STD are located outside the area covered by this map, their directions and distances to the crater are indicated with yellow arrows. The approximate extent of the crater glacier is shaded in blue; the area covered in Figure 10 is marked by the dashed red box.

1.3. Seismicity and Deformation at Mount St. Helens

Here we systematically analyze optical camera data from Mount St. Helens collected over a 6 week period in the summer of 2006. We use modern image correlation techniques and a new approach that allows the extraction of 3-D displacements from multiple camera perspectives, based on reprojecting pixel displacement fields on a high-resolution digital elevation model (DEM) [James *et al.*, 2006, 2016]. This study focuses on the identification and quantification of short-term pixel displacements and the seismicity, exploring their relationship in time and magnitude. We integrate data from multiple cameras into a common reference frame and systematically compare high-resolution measurements of displacements to seismic data. Our results provide new insights into the internal mechanics of dome growth at Mount St. Helens and the origin of the processes underlying the seismic signals.

2. Data

2.1. Seismic Network

The seismic data used in this study were collected by the University of Washington Pacific Northwest Seismic Network and the USGS Cascades Volcano Observatory. We use predominantly the stations RAFT and SEP, accelerometers located close to the dome, as well as the short-period seismic station HSR located at a distance of 3 km (Figure 1). Data from the short-period seismometers SEP, SHW, and JUN, the accelerometer NED, and the broadband station STD were also considered. The accelerometers and short-period seismometers had a sample rate of 100 Hz, while STD was sampled at 50 Hz and has a sensitivity down to 60 s.

2.2. Camera Network

The images used in this study were acquired by Olympus C30-30 digital cameras installed by the USGS Cascades Volcano Observatory (CVO) as part of the remote camera monitoring system [Poland *et al.*, 2008; Major *et al.*, 2008, 2009]. The perspectives of the dome that the three cameras offer are shown in Figure 2. The Brutus and Sugarbowl cameras viewed the dome from similar directions, while the South Rim camera was installed on the opposite side of the dome. The different viewing directions of the cameras allow a relatively complete coverage of the dome, comparisons between observations, and a detailed record of observed pixel displacements for linking to seismicity.

The temporal resolution of our deformation measurements is dependent on the frequency of the image acquisitions. At Mount St. Helens, the cameras were acquiring images at regular intervals ranging from every

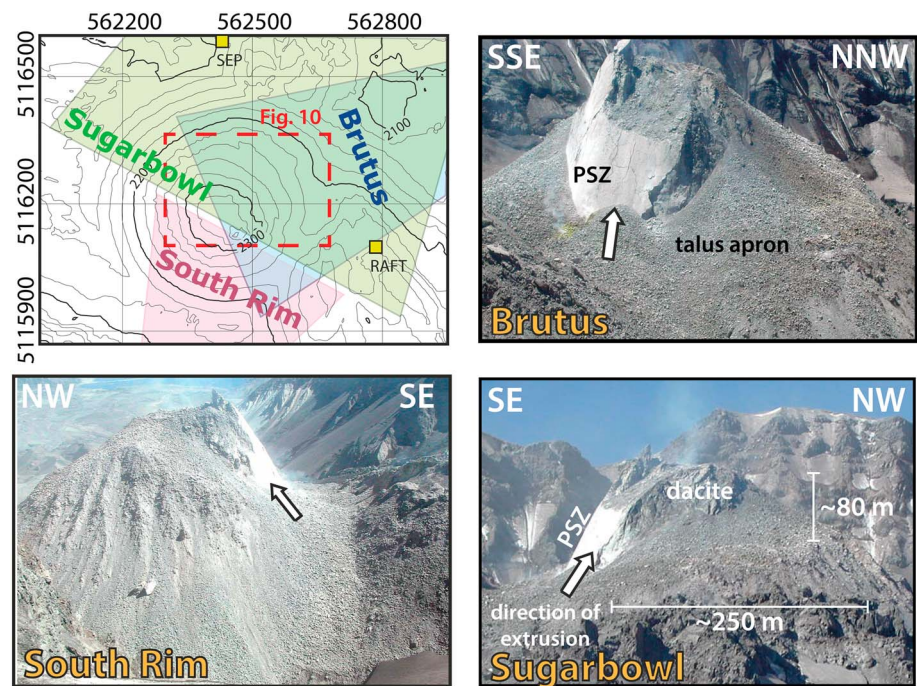


Figure 2. Contour map of dome (25m intervals) with approximate fields of view of the cameras covered by the original images. Photographs taken on 8 July 2006 were cropped for this figure to show the view on the dome in detail. The smooth or striated surface of the exhumed conduit fault is indicated as “Principal Shear Zone” (PSZ); the arrows show the direction of the extrusion in the perspective of the camera. The red box outlines the area covered in Figure 10.

15min to 1h, depending on the camera setup. Additionally, the temporal resolution of our measurements is affected by visibility and time of the day, since images where the dome is obscured by clouds or strongly overexposed have to be discarded. Naturally, images taken during the night cannot be used.

The spatial resolution of our deformation measurements is dependent on the pixel size reprojected on the dome surface, which varies with the camera setup (zoom and image resolution), distance, and orientation to the target. The images used here had a resolution of 1280×960 pixels. For pixels projected onto an orthogonal surface at the distance of the dome, the footprints were calculated to be around 70 cm for Sugarbowl and 35 cm for Brutus using calibration targets captured at close range [Major *et al.*, 2009]. No such published calibration is available for the South Rim camera. Considering the sensor specifications, distance to the dome, focal length, and image resolution, we calculate an approximate pixel footprint of 38 cm.

The cameras were set to a higher resolution (2048×1536 pixels) toward the end of July. Of the events included in the systematic study (see Table 1), only two (Events No. 41 and 42) were acquired with the higher resolution. For consistency, they were resampled prior to the Digital Image Correlation (DIC) analysis.

3. Methods

3.1. Digital Image Correlation

DIC is a computational method used to calculate the 2-D displacement field between two successive images [Pan *et al.*, 2009]. In the case presented here, the method relies on naturally occurring intensity patterns visible on the rough surface of the dome. The images are first converted to a 2-D matrix of intensity values and coregistered at subpixel level using a reference area outside the deforming area (e.g., on the crater wall or the 1980s dome). The images are then divided into a grid of discretized overlapping subregions (see Pan *et al.* [2009] and section 3.2). For each subregion, the displacements relative to the reference image are calculated by optimizing a fast Fourier transform-based cross-correlation function. We use the StrainMaster package developed by LaVision, which allows for multiple sequential passes with decreasing window sizes and varying amounts of overlap, which iteratively improves the displacement calculations for each subregion. Erroneous displacement vectors are removed based on their low correlation values as well as median filtering [Westerweel, 1994].

Table 1. Seismic Events and Camera Data Analyzed and Results of the Spectral Amplitude and Displacement Calculations^a

No.	Event Date	Event Time	SA_{EQ}	SA_{Trem}	South Rim ^b			Brutus		
					im1	im2	D_M (Pixel)	im1	im2	D_M (Pixel)
1	2006/6/24	12:36:50	9.6	7.78	12:44	12:59	1.7	12:24	12:44	–
2	2006/6/25	03:38:10			03:59	04:14	–	03:10	04:10	–
3	2006/6/25	03:57:20	6.57	4.02	03:44	03:59	1.6	03:10	04:10	–
4	2006/6/25	23:58:55	36.9	11.9	23:59	00:29	2.4	23:24	00:11	1.2
5	2006/6/26	04:35:45			04:29	04:59	–	04:24	04:44	–
6 ^c	2006/6/26	22:57:10	26.4	7.82	22:44	23:29	–	22:44	23:04	1.6
7	2006/6/28	03:12:40	20.5	5.9	03:14	03:29	1.6	23:11	04:04	–
8	2006/6/28	14:39:00			14:14	15:14	–	14:24	15:10	–
9 ^c	2006/6/29	17:48:55	17.2	1.75	17:29	18:44	1.0	17:44	18:04	0.83
10	2006/6/29	19:26:16			18:44	20:14	–	19:10	20:10	–
11	2006/6/29	20:47:19	14.1	4.25	20:14	22:59	1.2	20:10	21:10	0.63
12	2006/6/30	01:32:00			01:29	01:59	–	01:24	01:44	–
13	2006/6/30	12:00:20	4.7	2.49	11:59	12:14	1.1	11:44	12:04	–
14	2006/6/30	17:01:40			16:59	17:29	–	16:44	17:10	–
15	2006/7/1	15:00:45			15:08	15:38	–	14:23	15:10	–
16	2006/7/3	17:26:40			17:08	18:08	–	17:10	18:11	–
17	2006/7/4	00:35:20			00:23	01:08	–	00:10	01:10	–
18	2006/7/4	15:47:39			15:38	16:08	–	15:23	16:10	–
19	2006/7/4	22:32:30	14.6	7.37	22:38	22:53	1.6	22:10	23:10	1.0
20	2006/7/5	02:39:09			02:38	03:08	–	02:10	03:10	–
21	2006/7/5	16:22:50			16:08	16:53	–	16:10	16:43	–
22	2006/7/6	02:36:20	30.8	10.1	02:38	02:53	2.4	02:11	03:10	1.2
23	2006/7/7	16:29:40	17.9	9.53	16:33	16:53	1.7	16:10	17:10	1.0
24	2006/7/7	17:23:10			17:13	17:53	–	17:10	18:04	–
25	2006/7/8	13:18:30			13:13	13:43	–	13:10	13:23	–
26 ^c	2006/7/8	16:47:20	20.1	5.51	16:33	17:23	–	16:10	17:10	2.0
27	2006/7/9	03:02:30			03:02	03:32	–	02:43	03:10	–
28	2006/7/9	12:56:40	25.2	13.1	13:02	13:22	2.3	12:11	13:11	1.6
29	2006/7/9	14:00:30			14:02	14:32	–	13:11	14:11	–
30	2006/7/11	00:37:20			00:33	01:03	–	00:03	00:43	–
31	2006/7/11	01:22:30	7.19	7.76	01:23	01:43	1.8	00:43	02:10	–
32	2006/7/13	12:38:10	8.93	5.19			N/A	12:11	13:11	1.3
33	2006/7/14	21:27:20	24.8	13.5			N/A	21:24	21:44	1.1
34	2006/7/15	20:07:20	9.91	19.6			N/A	19:11	21:11	1.0
35	2006/7/17	01:29:10	33.2	11.1	01:33	01:43	2.3	00:10	02:10	1.6
36	2006/7/18	00:47:00	10.3	9.72	00:54	01:04	2.0			N/A
37 ^c	2006/7/18	16:55:50	76.8	7.70	16:54	17:54	1.8	16:11	17:04	1.9
38	2006/7/19	13:20:50			13:24	13:44	1.1?	12:24	13:44	0.97
39	2006/7/23	04:16:10	9.43	4.57	04:07	04:27	1.4	04:11	04:24	0.79
40	2006/7/24	18:39:30	25.6	11.6	18:27	19:07	2.4	18:24	18:44	1.2
41	2006/8/5	16:45:40	24.9	21.3	16:37	17:07	3.2	16:10	17:10	1.8
42 ^c	2006/8/5	20:15:20	71.9	7.9			N/A	20:10	21:10	1.5

^aFollowing 2006/07/11 only events associated with displacements are shown. SA_{EQ} , average spectral amplitudes of leading earthquake; SA_{Trem} , average spectral amplitudes of tremor; D_M , mean amplitude of pixel displacements; im(1,2), time of image acquisition (internal camera clock); N/A, no suitable imagery available or noisy results in the DIC analysis; –, no displacements detected by DIC.

^bThe internal clock of the South Rim camera time is approximately 13min early; the pixel displacements therefore appear to be delayed relative to the seismic event (see section 5.1.1).

^cEvents involving displacements in the L region.

Under ideal conditions, DIC can allow displacement calculations with an accuracy of a fraction of a pixel [Pan *et al.*, 2009].

DIC has become a common remote sensing tool for measuring deformation using terrestrial optical camera systems in a wide range of settings, including volcanoes [James *et al.*, 2007; Johnson *et al.*, 2008; Walter, 2011; Walter *et al.*, 2013b], landslides [Travelletti *et al.*, 2012], and glaciers [Rosenau *et al.*, 2013; James *et al.*, 2016], taking advantage of the low cost, easy hardware installation, and its flexibility concerning temporal and spatial resolution. In particular, DIC offers the possibility of measuring displacements at variable time resolutions, covering both the slower and regular displacements as well as short-term deformation as expected during an earthquake, which makes it a good tool to study deformation at volcanic domes.

3.2. Database Compilation

Due to the overall good weather and availability of data from multiple cameras, we chose a period between the end of June and end of July 2006 for this study. During this time period, earthquakes consisted of two types: small-amplitude earthquakes occurring at rates of two or more per minute and larger-amplitude earthquakes ($M > 1$) that occur approximately three to four times per day. The earthquakes of interest were initially identified based on a threshold of 150 counts ($\sim 11 \mu\text{m/s}$, assuming a flat response) in the HSR records, which adequately distinguished the larger earthquakes from the smaller drumbeat earthquakes. HSR was used, despite being at a distance of 3 km to the dome, since it was easy to identify the stronger earthquakes above the background noise of that station, while the stations close to the dome contained many types of seismic signals associated with dome growth (i.e., rockfalls, drumbeat earthquakes, etc.). Apart from a few exceptions (e.g., Event No. 13 or 31 in Table 1), most of the events we identify can also be found in the Pacific Northwest Seismic Network catalogue.

Out of the list of picked events, only those occurring during daylight (approximately 11:30am to 04:30am (of the following day) UTC) were considered. The image database was then explored to identify those events where data are available from the South Rim *and* Brutus cameras, since these cameras offered the highest resolution on the dome surface. The images bracketing the seismic event were then analyzed using DIC. The size of the correlation windows used in the DIC varied between 12 and 24 pixels, depending on the amplitude of the pixel displacements to maximize the quality of the DIC result. Adjacent windows overlapped by 75%, yielding pixel displacement fields of up to 320 by 427 vectors.

An event was considered to show no dome displacement only when images from *both* the South Rim and Brutus cameras were available and the DIC results from both cameras showed no displacement. In order for an event to qualify as showing deformation, a clear signal from one camera would suffice (Figure 3).

The clarity of the DIC-derived displacement fields varies between image pairs. Three types of noise may be observed in the DIC results: random noise (the displacement vectors being randomly oriented), spatially correlated noise (identical displacements of neighboring pixels over a larger area), and correlation failing due to changes in the surface pattern (i.e., detachment of material by rockfalls or an internal reorganization of the clasts). When the correlation is poor, the displacement vectors corresponding to those areas of the image do not pass the sequential quality control in the processing software where we discard vectors with low correlation values or large deviation from their neighbors. Therefore, no displacements can be extracted in those parts of the image.

The amount of random and spatially correlated noise depends mainly on the light conditions and the amount of time elapsed between the images and may also occur if an image is disturbed by haze. Furthermore, images acquired at different lens apertures may lead to apparent pixel displacements due to lens distortions. We minimize this noise by using image pairs which are optically consistent. In some cases this requires skipping one image in the acquisition sequence, therefore increasing the temporal baseline between the images to be correlated. However, in order to restrict the contribution of the regular dome extrusion to the pixel displacements related to the earthquakes, we only allow for a maximum interval of 2h between images.

In general, displacements below 0.4 pixel are discarded as noise, which roughly corresponds to the mean 2h pixel displacements we derived from daily images (supporting information Figure S1). Image pairs with high levels of noise (correlated, random, or due to low correlation) were discarded as inconclusive. Overall, 50–60% of the initially picked 66 seismic events occurring between 25 June and 11 July were excluded from further analysis.

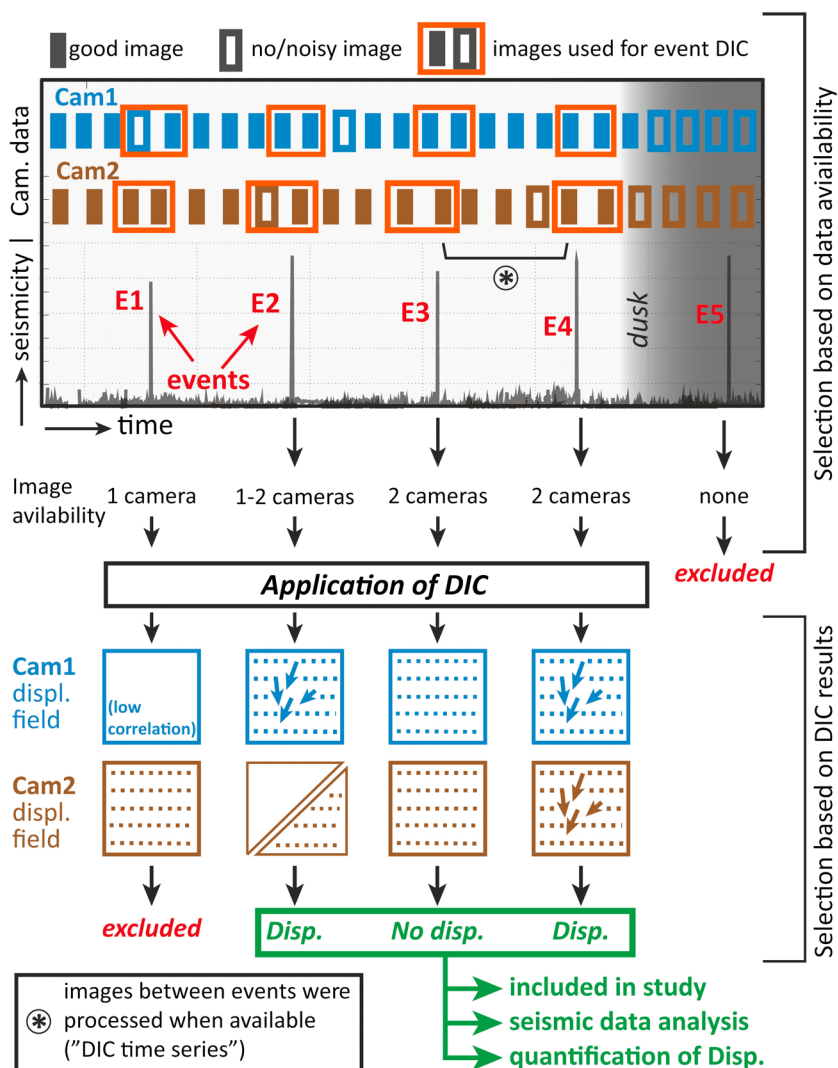


Figure 3. Workflow for compilation of event database illustrated on a schematic seismic and two hypothetical camera data sets (Cam1 and Cam2). See text for details.

3.3. Calculation of Mean Pixel Displacement and Spectral Amplitudes

Following the above routine, we compiled a catalogue of events which were either clearly associated or not associated with detected pixel displacements (Table 1). For the events associated with displacements, a polygon mask was applied manually to the displacement fields to enclose the area affected by displacements, excluding the sky and other areas lying in the background. From within the polygon, all vectors with magnitudes smaller than the noise threshold were removed. The remaining vectors were then used to calculate the average pixel displacement amplitude and the pixel area affected by displacements.

Subsequently, we analyzed the seismic records of the events associated with displacements for their power spectra and mean spectral amplitudes as a measure for seismic energy release. When the high-amplitude earthquake is followed by tremor, we may separate the leading earthquake from the tremor by considering different spectral bands. For the leading earthquake, peak frequencies were between 1 and 5 Hz, and thus, we calculated the mean of the amplitude of the fast Fourier transform within that band. Similarly, the energy of the tremor was localized between 5 and 20 Hz, and we used that range to calculate the mean spectral amplitude of the tremor. This analysis was performed for the stations SEP and RAFT; however, the data from RAFT were most complete during the time period of our study and thus preferred for comparison with mean pixel displacements. Due to the limited dynamic range of the instruments, the signals of the leading earthquake may clip, in particular in the stations close to the dome. However, the signal is well behaved during the tremor phase, which is the focus of this paper.

3.4. Calculation of 3-D Displacements

The fixed cameras record a two-dimensional and unidirectional field of view. When the target is viewed from similar perspectives, a stereo-matching approach can be applied to enable the DIC-derived displacement fields to be converted from image space (pixels) into 3-D space. However, this can rarely be done in natural settings, since suitable locations for camera installations which enable efficient stereo matching are rare. Also, larger viewing angles between cameras are generally preferred to enhance coverage, whereas smaller angles are needed for stereo matching. Despite the Sugarbowl and Brutus cameras covering similar areas of the dome, the angle between them is still too large to extract full 3-D displacement fields using a stereo-matching DIC approach. Manual identification of individual features on the dome can enable some 3-D deformation to be extracted from multiple camera images [Major *et al.*, 2009], but this sacrifices the high spatial resolution DIC offers.

Instead, we develop a new technique that allows 3-D deformation maps to be determined from DIC analyses of multiple cameras when stereo matching fails. The approach is based on reprojection on a high-quality DEM [James *et al.*, 2016] and results in 3-D displacements calculated for those areas of the DEM which are covered by the DIC-derived displacement fields from two (or more) cameras. First, the orientation of the Sugarbowl and Brutus cameras is determined by aligning them to the DEM. To identify the areas on the dome which are visible from both cameras, we reproject the image points representing each Sugarbowl camera pixel onto the triangulated DEM, to derive their 3-D coordinates. Any of these 3-D points that are not visible in the Brutus camera are then discarded. For the remaining points, their equivalent displaced image positions are determined from the DIC results for both cameras and are then reprojected. This results in two rays for each displaced point, so that displaced 3-D coordinates can be derived by ray intersection. Thus, the displaced 3-D point coordinates are not derived directly by reprojecting onto the DEM surface. We determine the 3-D displacement vectors by the difference between the original 3-D points and their displaced equivalents.

Due to the rapidly changing topography of the Mount St. Helens dome, we can only calculate reliable 3-D maps for events that occurred close to the time when a DEM was acquired. For other times, the lack of an accurate DEM of the dome surface would result in unknown and systematic error in the reprojection and intersection calculations. The DEM acquisition that is closest to the period studied was on 18 August 2006 [Messerich *et al.*, 2008]. A significant seismic event associated with deformation of the dome occurred the following day, making it an ideal candidate for the 3-D displacement calculation. Furthermore, we can use the image data of the days surrounding the DEM acquisition to calculate the daily 3-D surface displacements and the effect of the seismic event on the measured dome velocities.

3.5. DIC Time Series

In order to detect any rapid changes occurring on the dome in the absence of a seismic signal, we perform a DIC analysis of the camera data independently of our seismic catalogue. We processed all the July 2006 data from the Brutus and South Rim cameras at 30min to 1h image intervals using DIC and visually inspected the pixel displacement fields for short-term deformation on the dome. We note that this analysis is incomplete, since the image sequence was interrupted by periods of no visibility. However, several hundred hours of useful camera imagery were examined.

4. Results

Our analysis revealed the repeated occurrence of pixel displacements in the camera imagery related to the seismic events in our catalogue. Out of the 42 seismic events included in this study, 25 were found to be associated with measurable displacements on the dome (Table 1). Based on the DIC time series (section 3.5), we did not detect any short-term pixel displacements on the dome in the absence of seismic events.

We will first describe the differences in the seismic records between the events associated with displacements and those that were not. We then describe the DIC results of the coseismic displacements in detail and the relationships between the seismic and deformation signals. Finally, we will present the results of the 3-D calculations for the event on 19 August 2006.

4.1. Seismicity: Differences Between Events

The analysis of the seismic data showed strong differences between the events associated with pixel displacements and those that were not.

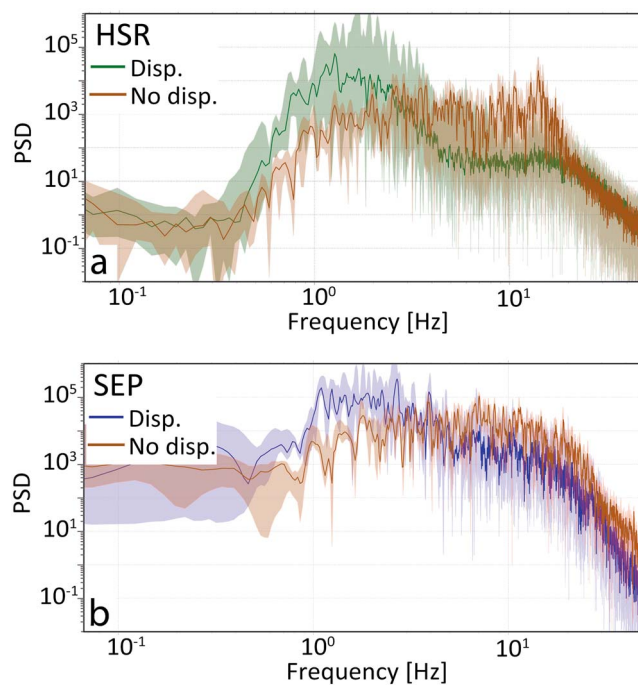


Figure 4. Power spectral densities of earthquakes associated and not associated with displacements for the seismic stations (a) HSR and (b) SEP. The solid lines show the median PSD; the shaded envelopes correspond to the minimum and maximum values. In order to reduce the contribution of the tremor following the leading earthquake, we only include the first 20 s after the onset of the event into the calculation. We used events No. 2, 8, 14, and 25 in Table 1 (no displacements) and No. 1, 3, 6, and 9 (with displacements). The corresponding waveforms are displayed in supporting information Figure S2.

event. Many of these events also had relatively large amplitudes, although several small events were also associated with pixel displacements (e.g., Events No. 11 and No. 13 in Table 1). The tremor itself is of high frequency and only visible in the seismic records from stations located in immediate proximity to the dome (Figure 6), suggesting a surface source with poor seismic coupling, such as a slumping or a rockfall. The duration of the tremor ranges from around 1 min to several minutes long. In some cases, events lacking displacements were also followed by tremors (Figure 7); however, it was considerably weaker than the tremor observed during the events with displacements.

4.2. DIC Results

Our study falls into a period of active dome extrusion. When analyzing images on a daily basis, the displacement fields are characterized by upward and lateral displacements in the camera fields of view (see supporting information Figure S1). When displacements occur in association with seismic events, however, the DIC results show only downward displacements, in some cases with a lateral component. Figure 5 (right column) shows the pixel displacement fields from the Brutus and South Rim cameras for two selected events. (Events No. 9 and No. 11). The background colors show the amplitude of the displacement vectors in pixels, and the arrows show the direction of the displacements in the camera field of view.

The displacements on the dome are clearly visible from both camera perspectives. Their amplitude generally increases toward the center of the area affected by the displacements, reaching maximum amplitudes which exceed 1.5 pixels. The pixel displacements observed from South Rim are generally larger than those observed from Brutus. During Event No. 9, the area affected by displacements in the Brutus camera is approximately 80m across, with displacement amplitudes of around 40 cm; however, an appropriate conversion from pixels to meters and resolving the full 3-D displacement field is only possible when applying our new method (section 4.4).

4.1.1. Power Spectral Density

The power spectral density (PSD) of events showing displacements had a lower frequency signature when directly compared to events without displacements at the same seismic station (Figure 4). The differences appear stronger in the data from station HSR (Figure 4a) than in those from SEP (Figure 4b). This may be due to the greater distance of the station HSR to the dome and the stronger attenuation of the higher frequencies with greater distance. At HSR, the events associated with pixel displacements show a strong component around 1 Hz, similar to the low-frequency events described in *Horton et al.* [2008] and *Moran et al.* [2008b].

The seismic signals of events that did not show any displacements in the camera imagery (plotted in brown in Figures 4a and 4b) had higher-frequency signatures, lacking the peak at around 1 Hz, and were more similar to the tectonic events described in *Horton et al.* [2008].

4.1.2. Occurrence of Tremor

The events showing pixel displacements in the camera imagery were all followed by a prominent broadband tremor-like signal (Figure 5), which started between 10 and 40 s after the onset of the main

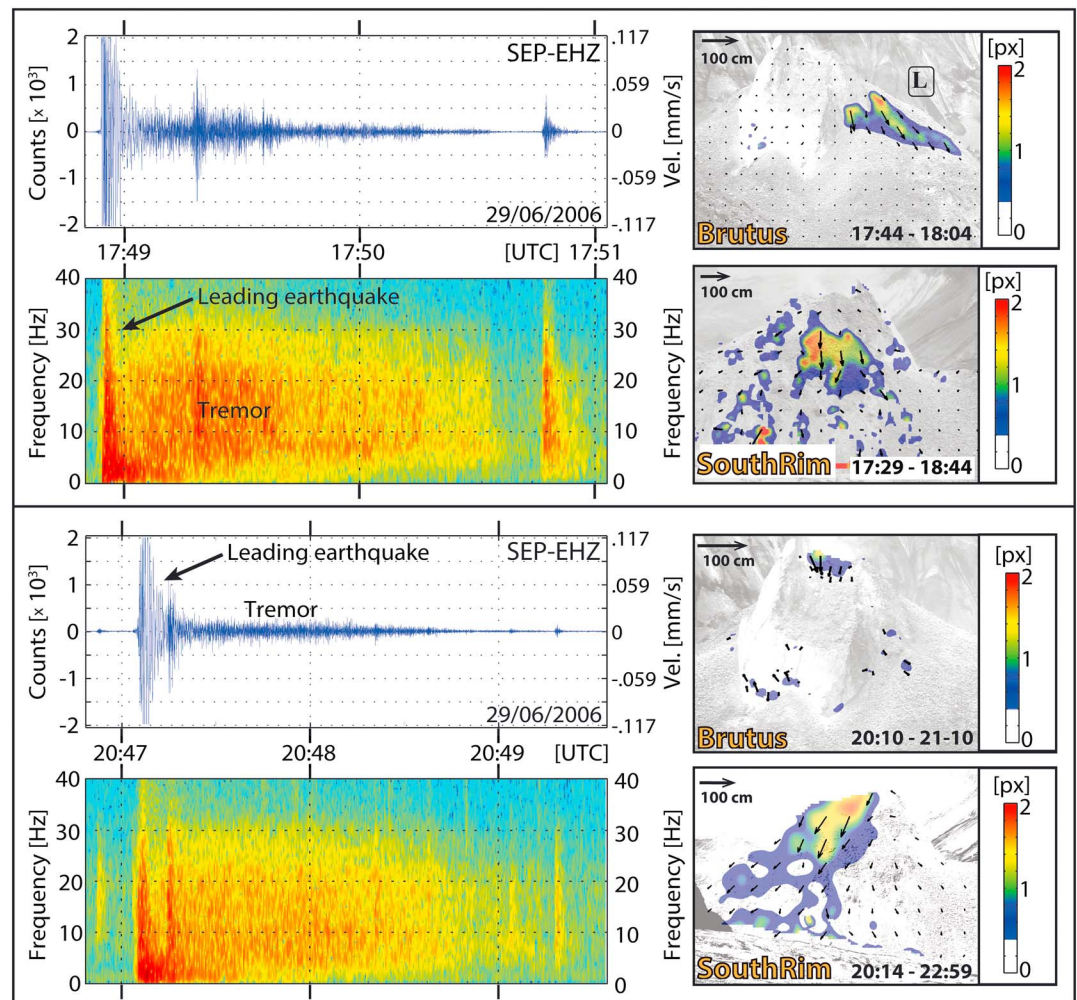


Figure 5. (left column) Trace and spectrograms from seismic station SEP showing two examples of events associated with dome displacements (Events No. 9 and No. 11 in Table 1) and (right column) the associated pixel displacements calculated from Brutus and South Rim images. The arrow corresponds to 100 cm of displacement along a projected surface at the distance of the dome. Due to the proximity of the station to the dome the signal in the initial phase may clip; however, we note a concentration of low-frequency energy at the beginning of the event and the strong broadband tremor following the main earthquake.

The DIC displacement fields show two distinguishable areas of differential motion of the dome. One area is located around the top of the dome, well visible from South Rim, but often also from Brutus. Pixel displacements in the central areas of the dome are observed in both events in Figure 5.

The second area is located laterally, toward the right side of the Brutus images (north), involving more of the talus apron. This area is not visible from the South Rim camera and appears as a triangular surface in the Brutus displacement fields. The first event in Figure 5 also shows displacements in this region, which has been labeled as lateral (“L”) region. Most of the events we analyze in this study show displacements in the central region of the dome; only five involve the *L* region. These were indicated with footnote c in Table 1. During some events (e.g., Events No. 9 and No. 37), both the central dome and the lateral area would show displacements. Other events would only be associated with displacements in the *L* region but not in the central dome (e.g., Events No. 6 and No. 26).

We note that all the displacements we observed occurred within the dome in the area behind the exposed edge of the dome that represented the exhumed conduit fault (visible as the smooth surface in the images). None of the events presented here showed any pixel displacements on the smooth or striated surface of the fault.

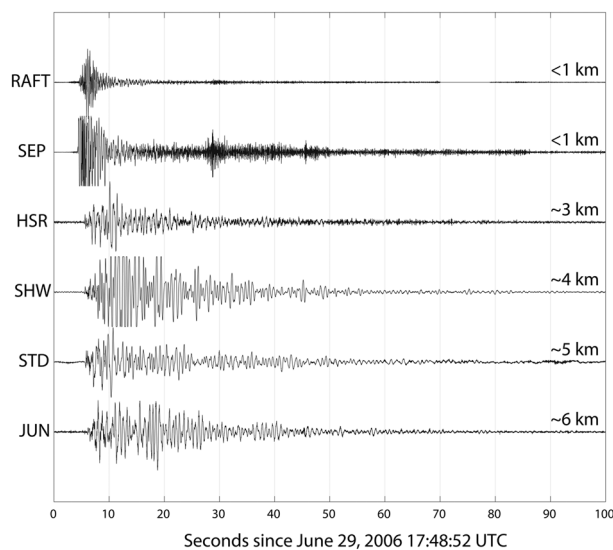


Figure 6. Record section for event No. 9 in Table 1. Labels are approximate distances from the source.

The DIC results of events lacking displacements only involved uncorrelated noise, usually below the level of 0.4 pixel (Figure 7). No measurable and coherent displacements on the dome were observed to be associated with any of the higher-frequency events—even the larger-amplitude events or events followed by tremor. However, *all* lower frequency events for which suitable images were available were associated with displacements.

4.3. Spectral Amplitude Relationships

We calculate the mean spectral amplitudes of the leading earthquake and the tremor and the mean displacements in the Brutus and South Rim cameras following the method described in section 3.3 in order to evaluate possible links between the causative processes.

4.3.1. Earthquake and Tremor Spectral Amplitudes

We observe no clear relationship between the average spectral amplitudes of the leading earthquake and the average spectral amplitude of the subsequent tremor (Figure 8). Using the camera data, we can distinguish between events which only show displacements in the central dome region (plotted in blue) and those involving displacements in the *L* region (plotted in red). We note that the two largest earthquakes analyzed in this study (Events No. 37 and No. 42) were associated with displacements in the *L* region. However, they were not associated with particularly strong tremor (red outliers in Figure 8). Also, relatively small leading earthquakes may be associated with very strong tremor if the displacements occur only in the central area of the dome (blue outliers in Figure 8).

We interpret this result as the generation of the tremor being mechanically different, depending on which area of the dome is affected by the displacements. The 3-D calculations (section 4.4) show that displacements in the *L* region have an overall smaller vertical component when compared to the central areas of the dome. Events affecting the central region of the dome show a wider range of tremor amplitudes, including high-amplitude tremor. Differences in the efficiency of generating high-amplitude tremor may be due to a shallower dip on an underlying fault plane or due to temperature-dependent rheological differences resulting from the larger distance of the *L* region to the hot dome core. Due to the different behavior behind the tremor generation in the *L* region and the central regions, we only consider events with displacements occurring exclusively in the central dome area for the comparison between spectral amplitudes and pixel displacements.

4.3.2. Mean Displacements and Spectral Amplitudes

We compare the mean displacements visible in the South Rim and Brutus cameras to the average spectral values of the leading earthquakes and the subsequent tremor for each event (Figure 9). This analysis reveals an apparently linear relationship between the mean pixel displacement magnitude at the South Rim camera and the mean tremor spectral amplitudes. The *R*-square values for a linear fit (plotted in red in Figure 9) are considerably lower for the Brutus camera, possibly reflecting a lower signal-to-noise ratio due to the orientation of the surface of the upper central dome relative to the camera, which gives a smaller pixel footprint.

The loose relationship between the amplitudes of the leading earthquake and the tremor (Figure 8) leads to similarities in the patterns when plotting either the leading earthquake or tremor spectral amplitudes against the displacements (Figure 9). However, in all cases, the scatter is reduced and the *R*-square values increased when comparing the displacements against the tremor amplitudes (right column) rather than the earthquake amplitudes (left column), suggesting a closer link between the tremor and the displacements.

In the framework of this study we have also calculated the area of pixels affected by displacements, as well as the “area-integrated displacement” by multiplying the pixel area by the mean displacement. However, we found no correlation between these measurements and the spectral amplitudes of the seismic signals.

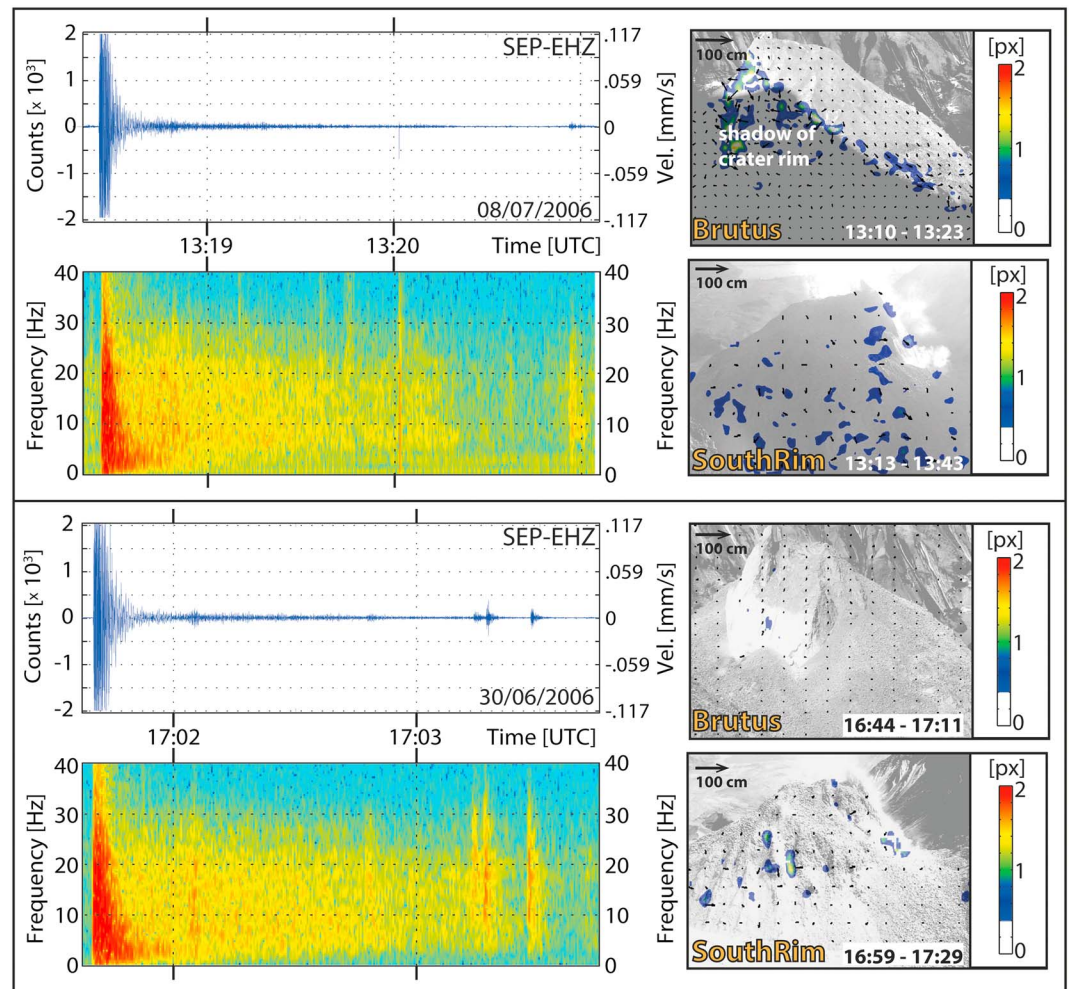


Figure 7. Trace, spectrogram, and DIC results from events lacking displacements (Events No. 25 and 14 in Table 1). Similarly to Figure 5, the signal of the leading earthquake may clip. The events lacking displacements only show weak tremor and no clear concentration of low-frequency content at the event onset when compared to the events with displacements (Figure 5).

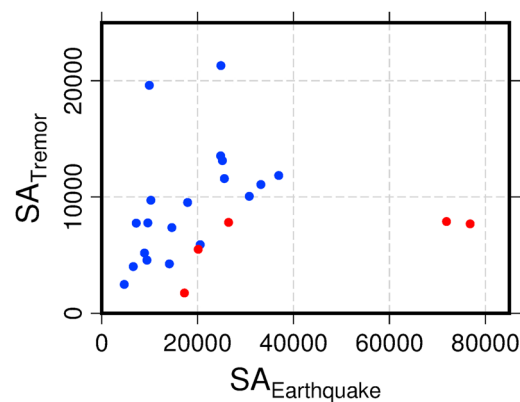


Figure 8. Average spectral values of leading earthquake spectral amplitudes ($SA_{\text{Earthquake}}$) plotted against the tremor spectral amplitudes (SA_{Tremor}). Values associated with deformation in the L region are plotted in red.

4.4. Results of 3-D Calculations

We use a DEM of the crater floor acquired on 18 August [Messerich *et al.*, 2008] and the displacement fields calculated by DIC from two cameras to extract a full 3-D deformation field for an earthquake that occurred on 19 August, the day following the acquisition of the DEM. Due to the need for an accurate DEM and the rapidly changing topography on the crater floor, we could only perform the 3-D calculation for this particular event.

Figure 10a shows the details of the seismic signals and the single-camera displacement fields. The spectrogram is similar to those in Figure 5, albeit the event used in the 3-D calculation was of larger magnitude. The higher-resolution setting of the cameras at the end of July also contributes to the large

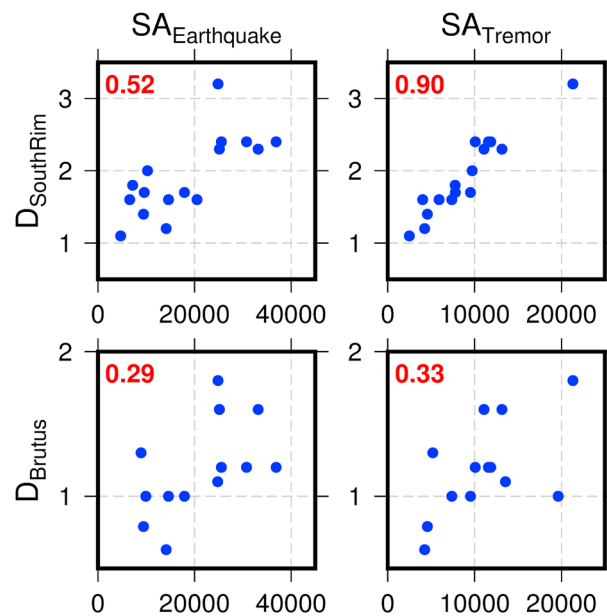


Figure 9. Plots showing relationships between mean pixel displacements from Brutus and South Rim cameras (D_{SouthRim} and D_{Brutus}) against (left column) earthquake and (right column) tremor mean spectral amplitudes ($SA_{\text{Earthquake}}$ and SA_{Tremor}). The R -square values for a linear fit are plotted in red.

amplitude of the pixel displacements seen in the Brutus displacement field in Figure 10a when comparing it to those in Figure 5.

The results of the 3-D displacement calculation in a very close-up view of the dome are shown in perspective view (Figure 10b) and plan view (Figure 10c). The results cover the section of the dome that is visible from both the Sugarbowl and Brutus cameras. Since the perspective of the South Rim camera is not covered by the other cameras, it could not be used for the 3-D displacement calculation. For a larger field of view and orientations of the cameras relative to the dome refer to Figure 1.

The displacements during the 19 August event affected a large surface area of the dome. The diameter of the area of the dome that experiences vertical (downward) displacements greater than 40 cm exceeds 150 m. The western limit to the deforming area cannot be constrained due to lack of coverage by both the Brutus and Sugarbowl cameras.

The results of the 3-D analysis highlight the segmented fashion of the dome deformation during the earthquakes described in the previous section and allow estimation of the 3-D coseismic deformation field in very high detail. The displacements within the lateral area previously identified in the Brutus imagery (L region) are characterized by displacements toward the north reaching amplitudes of around 40 cm and vertical displacements of similar amplitudes. These displacements are clearly distinguished from the two areas to the south. The southeastern region (C_{Br}) displays very large vertical displacements of over 1 m, as well as horizontal displacements toward the NE of amplitudes in the range between 50 and 90 cm. The southwestern area (C_{SR}) displays mainly vertical displacements of around 40 cm but no horizontal motion.

Within the regions, the magnitude of the vertical displacements as well as the azimuth of the horizontal displacements are almost uniform. The boundary between C_{Br} and C_{SR} is very sharp, and we observe a sudden change of the observed horizontal and vertical surface displacements. The transition between the regions C_{SR} and L is marked by a narrow, east-west oriented feature where neither horizontal nor vertical displacements are visible on the dome surface (Figure 10c).

5. Discussion

Our results reveal that the steady dome growth at Mount St. Helens was repeatedly interrupted by downward displacements of the dome reaching magnitudes on the order of a meter over a timescale of minutes.

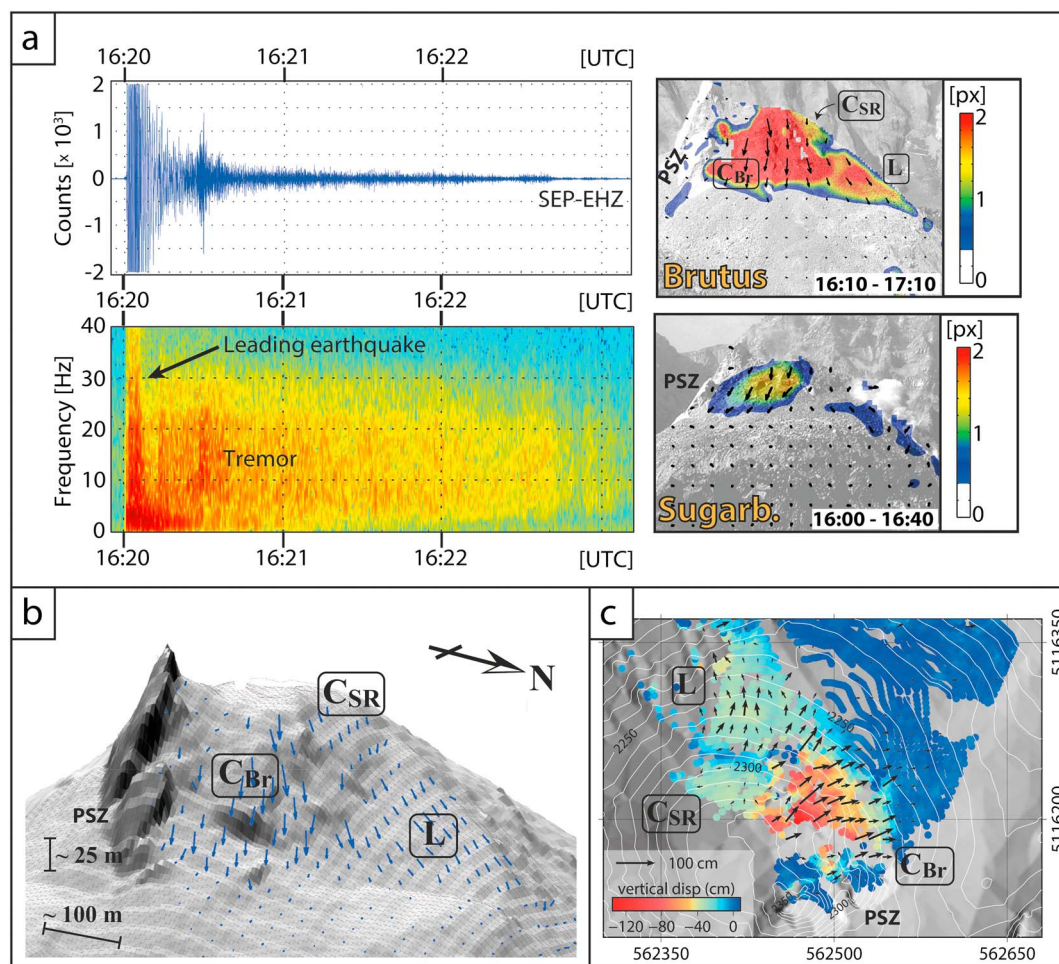


Figure 10. Results of 3-D calculations for 19 August event. (a) Traces and spectrogram from SEP station and DIC-derived displacement maps from Brutus and Sugarbowl cameras. The signal of the leading earthquake is clipped, yet we see the concentration of energy at around 1–2 Hz similar to the event shown in Figure 5. (b) Three-dimensional vectors plotted on the dome topography. (c) Top view on the shaded relief. The vertical displacements are plotted in color; the arrows show the horizontal displacements. The labels in red refer to the different dome regions (C_{Br} = central region visible from Brutus, C_{SR} = central region well visible from South Rim, L = lateral region visible from Brutus and Sugarbowl). “PSZ” refers to the exhumed conduit fault visible in all panels.

Measurable short-term downward pixel displacements were observed exclusively in combination with the occurrence of low-frequency earthquakes followed by high-frequency tremor. No short-term displacements were detected in the absence of such a seismic event, and all lower frequency seismic events in our database for which imagery is available from both the South Rim and Brutus cameras show pixel displacements as well as tremor. While some of the higher-frequency seismic events are also associated with tremor (e.g., Events No. 2, 8, 12, 27 in Table 1), none show displacements, despite some having relatively large seismic amplitudes (e.g., Events No. 2, 10, 15, 30 in Table 1). Therefore, our results strongly point toward the generation of the leading low-frequency earthquake, tremor, and dome displacements being linked by a common, repeatable mechanism.

We observe differential motion and strong segmentation into regions or “blocks” limited by narrow, well-defined boundaries suggesting that the shallow deformation is fault controlled. The areas in which displacements are observed are bound by the main conduit faults [Pallister *et al.*, 2013]. Within the deforming area, the segmentation occurs along internal dome structures. Such structures may form at deeper levels, for example, due to the development of shear bands [Hale and Wadge, 2008], internal stresses imposed by an oblique intrusion [Donnadieu and Merle, 1998], or slumping and spreading of a soft underlying material [de Vries *et al.*, 2000].

Our results suggest that such internal dome structures at Mount St. Helens controlled the deformation during the low-frequency earthquakes.

Rockfalls and the formation of dust-and-ash plumes were frequently observed in association with large-magnitude earthquakes at Mount St. Helens [Moran *et al.*, 2008a]. The frequency content of the tremor signals described in our study is also consistent with slumping or rockfall-like signals [Hibert *et al.*, 2014], and inspection of the optical data as well as areas of correlation loss in the DIC results show that rockfalls also occurred in some of the events analyzed here and therefore contributed to the seismic signal. However, due to the striking correlation between the mean displacement amplitudes and the mean spectral amplitudes of the tremor, the deformation of the dome appears to be the dominant source. The seismic signals we describe here have not previously been linked to deformation of the dome or the process generating low-frequency seismicity at Mount St. Helens.

Prior to discussing processes that may explain our observations, we briefly describe the main limitations of our work.

5.1. Data and Method Limitations

5.1.1. Camera Sampling Frequency and Clock Offset

The exact rate and timing of the displacements relative to the earthquake or tremor signals cannot be resolved, due to the low sampling frequency of the cameras. The presented displacement fields therefore usually cover a period of 20–30min surrounding the earthquake in the South Rim camera and up to 1h in the Brutus camera (Table 1). However, the duration of the tremor suggests that the displacements occur over a time span of tens of seconds to minutes.

Additionally, exploring the temporal relationship between the tremor and the displacements is complicated by an offset of the internal clock of the South Rim camera. We could constrain this offset to approximately 13min, i.e., the displacements in the imagery from South Rim appear to be delayed relative to the seismic and other camera data. This can be accounted for by choosing an appropriate “later” image pair for the DIC analysis.

5.1.2. Camera Resolution and Coverage

While DIC allows extraction of displacements at a much higher resolution than other methods, it is not sensitive to displacements smaller than 0.4 pixels (approximately 15 cm of displacement along a projected surface orthogonal to the Brutus and South Rim camera views). Also, we lack adequate camera observations from the western side of the crater (Figure 2).

Despite these limitations, under the working hypothesis that “Larger-amplitude, lower frequency events are associated with displacements, while higher-frequency ones are not,” all our samples fulfill this hypothesis. Lack of coverage and resolution does not appear to be an issue. Also, the “DIC time series” analysis (section 3.5) did not reveal any short-term displacements in combination with a tremor-like signal but lacking a leading earthquake. However, we cannot exclude that displacements below the detection threshold occurred.

5.1.3. Considerations for Future Installations

Future camera monitoring systems could be optimized for the detection and quantification of short-term dome deformation. More frequent camera acquisitions could increase the temporal resolution, potentially allowing a better understanding of the dynamics of the deformation process. This may also enable a larger number of events to be analyzed, in particular around dusk and dawn, by reducing the probability that one of the images is in the dark. A higher temporal sampling would also reduce the more subtle changes in the lighting conditions as well as the contribution of “regular” dome growth to the displacement signal and therefore the error in displacement calculations.

If images are acquired more frequently, the accuracy of the camera clocks becomes increasingly critical to constrain the timing of any displacement and its relationship to other high-rate geophysical data sets. Therefore, synchronization of the cameras with a GPS clock should be considered. Furthermore, a larger number of cameras, with greater overlap in the fields of view, as well as more frequent high-resolution DEMs acquired, e.g., from drone or helicopter overflights as routinely done nowadays, would allow 3-D displacement maps to be constructed for more seismic events.

5.2. Earthquake and Deformation Processes

In the following section we will discuss processes that may explain our observations. We can group the proposed mechanisms into two kinds:

1. Mechanisms that provide an explanation for both the leading earthquake and the displacements and tremor (“single-step mechanisms”)
2. Mechanisms that may explain the dome displacements and the timescale over which they occur but do not have the capacity for accumulating the strain needed to generate the leading earthquake. In these cases, we require a separate (independent) mechanism for the leading earthquake, and the observed displacements and tremor are related to the response of the dome to the passing seismic waves (“two-step mechanisms”).

5.2.1. Single-Step Mechanisms

5.2.1.1. Plug Stick Slip

Previous works have proposed that friction between the ascending plug and the conduit margin leads to the buildup of stress, which is released by shear failure during an upward “slip” of the plug during the low-frequency earthquake [Iverson *et al.*, 2006; Kendrick *et al.*, 2012, 2014]. Kendrick *et al.* [2012] also applied their model to one of the earthquakes included in this study (Event No. 42 in Table 1). According to their calculations, the coseismic slip would correspond to upward displacements of the dome in the range of 0.81 to 3.05 m. For motion occurring along a plane orthogonal to the viewing direction of the Brutus camera, this would correspond to 4 to 12 pixels of displacement, which lies well above our detection threshold of 0.4 pixel. However, we do not observe any upward displacements or large slip on the exhumed fault surface during any of the earthquakes. Our observations therefore do not support the Kendrick *et al.* [2012] model. Also, the apparent “stalling” of spine 7 in sequences composed of daily images, mentioned by Kendrick *et al.* [2012], appears to be not a real decrease in the extrusion velocity of parts of the spine but rather a superposition of the regular (upward) displacements and the coseismic (downward) displacements that occur during large earthquakes (see section 5.4). However, we note that the process described by Kendrick *et al.* [2012] may be taking place at greater depth, and the magnitude visible at the surface would be reduced if the plug is not rigid or is fractured between the earthquake source location and the dome surface.

5.2.1.2. Pressurized Crack Collapse

An alternative hypothesis for the LP seismicity at Mount St. Helens involves the repeated pressurization, collapse, and resonance of a steam-filled subhorizontal “crack” [Waite *et al.*, 2008; Matoza and Chouet, 2010; Matoza *et al.*, 2009]. Source mechanisms and locations were derived for earlier events, occurring in 2005. These were found to be dominated by volumetric moment tensor components and originated from a shallow aquifer in the southern area of the crater [Waite *et al.*, 2008; Matoza *et al.*, 2015]. A source process composed of a crack buried at shallow depth and episodically venting into the overlying loosely consolidated material through a network of fractures was also found to reconcile the observed seismic and impulsive infrasound signals [Matoza *et al.*, 2009].

We found similarities between events presented in our study and the two larger earthquakes studied in Waite *et al.* [2008]. The events occurring on 2 July 2005 (13:30) and 30 July 2005 (9:34) described by Waite *et al.* [2008] were both associated with tremor recorded only by the stations closest to the dome and included an initial long-period phase that closely resembles the spectra of the events we analyzed.

The displacements observed in our study are, however, constrained to the central region of the dome. If we apply the model of Waite *et al.* [2008] to the leading long-period part of the earthquakes, steam or magmatic gas would slowly accumulate and pressurize distinct regions or a network of fractures within the dome, possibly at the discontinuity associated with the crater floor. The low-frequency earthquake is generated as the threshold pressure in the expanding fracture network is exceeded, and the crack or fracture network collapses and degasses through the permeable upper dome. Following the evacuation and pressure drop, the dome pile at the surface collapses gravitationally (Figure 11a). The displacements observed in the camera data would reflect the structural adjustment of the fractured and loosely consolidated material above the crack to the new conditions, taking place over the duration of the tremor (tens of seconds to minutes). Such a sagging response of the dome to the evacuation of the crack has already been hypothesized by Waite *et al.* [2008]. We do not observe any inflation related to the slow pressurization and expansion; however, such a signal may be overprinted by the surface displacements related to the regular dome extrusion (section 5.4).

Our observations are, in general, consistent with this model. However, it remains arguable whether the fractured and porous material above the crater floor is capable of retaining a significant volume of gas under pressure. Also, in order to provide a repeatable source for the LP seismicity, a pressurized crack or fracture network located within the dome or conduit would have to be continuously reestablished, as it would otherwise move upward with the dome material.

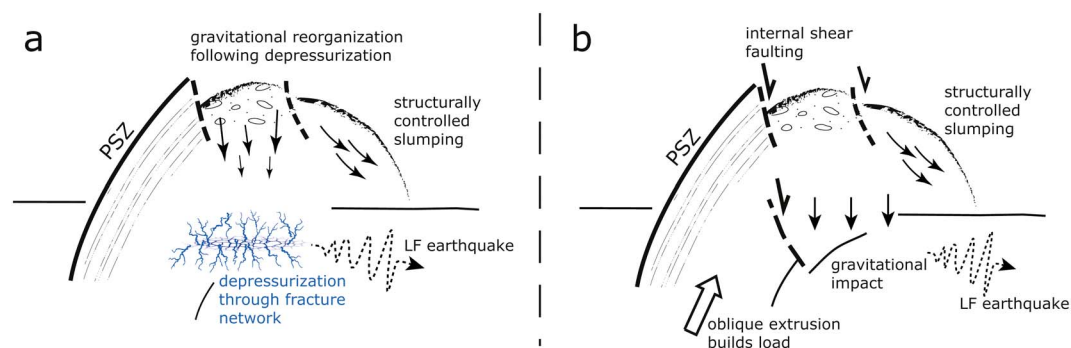


Figure 11. Mechanisms for generating the leading earthquake and displacements. (a) Mechanism driven by the collapse of a pressurized crack or fracture network, as proposed by previous authors. The evacuation and degassing of the “crack” generates the low-frequency earthquake; the overlying dome pile adjusts gravitationally in response to the pressure drop, generating the tremor and highlighting preexisting internal dome structures. (b) Mechanical collapse. The gravitational load and bending forces resulting from the oblique extrusion may generate the low-frequency earthquake by internally collapsing and impacting on the underlying material. The displacements are accommodated by internal shear faulting and shallow, structurally controlled slumping. Schematic and not to scale.

5.2.1.3. Mechanical Collapse

One might also consider a third mechanism, where the gravitational collapse is a driving mechanism and may generate both the leading earthquake and the displacements. This hypothesis is based on the gravitational load and the bending forces acting on the dome as it is being extruded at an angle, rather than vertically [Vallance *et al.*, 2008]. Above the solidification depth of around 1 km, the deformation was accommodated by brittle failure rather than viscous flow [Pallister *et al.*, 2013]. The accumulating load would lead to the buildup of stress on internal faults, which is released episodically by an internal breakup of the dome (Figure 11b).

In contrast to shear fracturing at the conduit margin [Holland *et al.*, 2011; Kendrick *et al.*, 2012], this mechanism involves shear failure within the dome. While this may be the source for the low-frequency seismicity, the gravitational impact of the overlying dome on the crater floor may also explain the mostly down first motions and volumetric components observed in the seismic data. While it may not be repeatable enough to generate the consistent drumbeat seismicity, this process could operate during the more irregular, larger-magnitude, low-frequency events. It would not require the trapping of gas or steam in a pressurized crack or fracture network and would also be reconcilable with the low gas content of the Mount St. Helens magma [Pallister *et al.*, 2008].

We cannot constrain whether the fault control that we can distinguish from the surface displacements reflects the upward propagation of the internal shear faults or rather shallow secondary features. Due to the ongoing extrusion and morphological changes, individual structures may not be long lived but instead redevelop in optimal orientations based on the current stress field.

5.2.2. Two-Step Mechanisms

The second class of mechanisms are not capable of generating the leading earthquake, yet they do have the potential for generating the observed surface displacements. The processes we briefly discuss below may act on temporal scales from tens of seconds to days, and displacements may be triggered when the dome material is agitated by the passing seismic waves of an independently generated earthquake.

Outgassing occurs when steam or gas that has separated from the magma rises and escapes to the surface or dissipates into the surrounding host rock, leading to compaction [Ichihara *et al.*, 2013; Matthews *et al.*, 1997] or fracturing at the conduit margin [Holland *et al.*, 2011]. While this may generate larger-magnitude earthquakes as described in section 5.2.1, it may also occur as a consequence of passing seismic waves triggering decompression and depressurization of deeper seated magma below the crater floor level. The gravitational readjustment or the dome pile above the conduit by structurally controlled slumping could explain the surface displacements we observe. However, the 2004–2008 Mount St. Helens dome dacite was notably gas poor and degassed at depth [Pallister *et al.*, 2008, 2013], with well-established degassing pathways along the conduit margin [Gaunt *et al.*, 2014]. Also, the camera data did not systematically show gas or steam plumes in association with surface displacements.

Viscous reorganization of the pores by relaxation of the surface tension may lead to densification while retaining high permeability of the magma. The importance of this process increases with smaller-scale pores and may contribute to deformation in particular over timescales of hours to years [Kennedy *et al.*, 2016]. The displacements we observe, however, take place over tens of seconds to minutes and thus fall outside this time frame. Also, the Mount St. Helens magma solidified at a depth of around 1 km below the vent, and above this level, deformation was entirely brittle [Pallister *et al.*, 2013].

The erupted material *thermally contracts* and densifies as it cools. Due to the timing of this study, however, we would expect a well-established thermal aureole around the conduit. Also, during the ongoing eruption the cooling magmatic column is constantly being replaced by new material. We can therefore consider the overall temperature gradients to be stable with thermal contraction only playing a minor role in the surface displacements.

In response to seismic shaking, *slumping* may occur when the unstable material of the dome pile slides downslope along shallow detachment planes or discontinuities, leading to slope-parallel components in the displacements. In general, we may expect a reaccumulation of the material at the bottom of the detachment plane, associated with a decrease in the vertical and an increase in the horizontal components of the displacement vectors. While we do observe slight changes in the components when going downslope in the L and C_{Br} regions (Figure 10), we cannot identify any accumulation or bulging at the bottom. However, due to the thin-skinned nature of the process, any accumulation can spread over a large area and occur outside the camera view. Slumping, controlled by shallow structures, is, however, a plausible mechanism, in particular considering the large slope-parallel components of the observed displacements in particular in the L region.

Repacking or settling of the erupted clasts or blocks may be triggered by the leading earthquake, gravitationally consolidating and increasing the static stability of the dome pile. This process decouples the time frame during which displacements occur from when the densification of the blocks takes place; i.e., viscous reorganization or slow outgassing may operate over hours (or even days) between the earthquakes, but the compaction of the pile as a whole occurs during seconds or minutes following the earthquake. In order for DIC to work, however, it is important that the pattern (and thus the relative orientation of the clasts) is stable between the images. If the clasts rotate individually, the pattern would change, reducing the correlation in that area and not allowing the calculation of displacements. Our results show that different areas of internally coherent competent rock move in the same direction, the pattern on the surface remaining the same, rather than loss of correlation due to internal reorganization of the clasts.

5.3. Conceptual Model

While some of the processes discussed in section 5.2.2 are tentative and likely to be triggered by seismic shaking, we point out that we do not observe any displacements associated with any of the larger-amplitude high-frequency earthquakes, which also have strong peak accelerations. If triggered outgassing or slow viscous pore reorganization played a significant role, we would expect to observe compaction and displacements accommodated by shallow slumping or settling also in association with the high-frequency events, which is not the case. We recognize that the dome structures may be more sensitive to lower frequency waves that travel along the conduit, producing surface waves and their amplitudes being enhanced [Neuberg *et al.*, 2000]. However, we favor a conceptual model that unifies all our observations.

We believe that our results leave room for various interpretations but propose that structurally controlled disintegration of the upper dome by faulting and slumping, as shown in Figure 11b, plays a dominant role. Degassing from a steam-filled fracture network at the crater floor level, as proposed by previous authors, is also possible, the displacements we observe being the integrated result of the gravitational response, albeit some questions remain open. Furthermore, combinations of these mechanisms (e.g., internal faulting opening pathways for gas propagation) also appear plausible. In either case, the potential contribution of gravity-driven dome deformation to the seismic and infrasound signals should be evaluated and considered in future studies.

5.4. Dome Extrusion Dynamics

The occurrence of seismic events linked to dome deformation has a strong effect on the measured daily extrusion velocities. We apply the 3-D method to calculate the surface displacements over 24 h. Since the pixel displacements need to be reprojected on the DEM, a good match between the images and the topography can only be obtained for the days surrounding the DEM acquisition on 18 August (section 3.4).

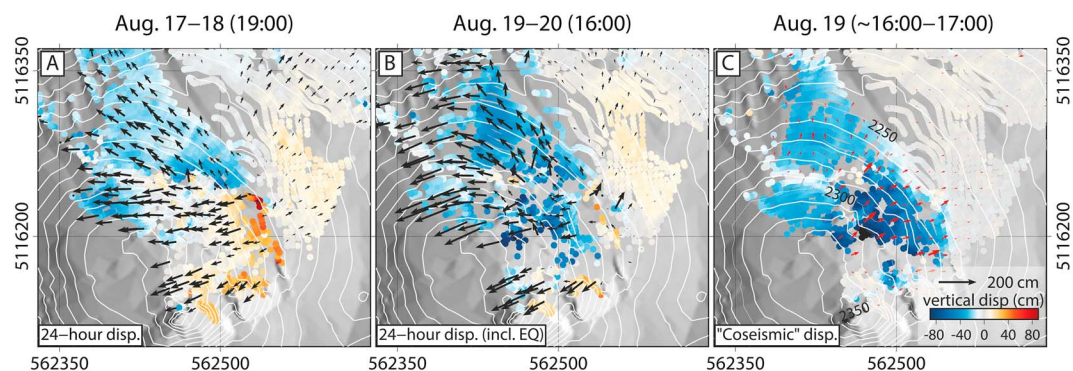


Figure 12. Daily 3-D displacements calculated from Brutus and Sugarbowl imagery for (a) 17–18 August and (b) 19–20 August. The 19–20 August displacements also cover the (c) 19 August event described in section 4.4. Color scale and reference vector for all three panels are given in Figure 12c and are saturated. Contour lines shown at 10 m intervals.

Figure 12 shows the 3-D surface displacements over three time frames. Figure 12a shows 24 h of “regular” dome extrusion between 17 and 18 August, during which no larger-magnitude, lower frequency events occurred. The displacements are marked by upward extrusion and translation toward the west and northwest, with the vertical components in the dome area reaching around half a meter, and horizontal components up to 1.5 m. Sudden gradients in direction and rate of displacements are indicative for partition of motion along internal dome faults.

The second time frame (Figure 12b) also covers 24 h but includes the large-magnitude seismic event from 19 August described in section 4.4. The short-term displacements during this event are also shown (Figure 12c, “Coseismic”). The displacements associated with the earthquake compensate for the regular growth in the central spine and significantly alter the 24 h displacement field.

Modern methods of volcano monitoring are increasingly providing high-rate observations of deformation at volcanic domes. However, when reaching a temporal resolution on the order of days, the displacements resulting from contributions from structural modifications and gravity-driven deformation may overprint or even dominate over any changes originating from processes such as variations in the injection rate of magmatic material or in the friction on the conduit faults. Isolating the relative contributions of these processes to measured dome deformation should be considered in future dynamic and kinematic studies and for better constraining experimental and computational models of dome extrusion.

6. Conclusions

Our systematic study of digital camera imagery of dome growth at Mount St. Helens in combination with the seismicity reveals that large-magnitude, low-frequency earthquakes were associated with strong vertical and downslope displacements of the upper dome material and a tremor-like signal, sometimes over several minutes long. The amplitudes of the tremor strongly correlate with the amplitudes of the observed displacements.

We demonstrate that these displacements occur only in combination with the low-frequency earthquakes and the tremor. This points toward a common underlying mechanism producing these three signals. We propose that the deformation we observe reflects the gravity-driven response of the dome to stresses imposed by the inclined extrusion or to depressurization. The tremor-like signal, recording the displacements of the dome, was observed only in the closest seismic stations. The proximity of the monitoring instruments to the dome is therefore critical for the investigation and correct interpretation of such shallow volcanic signals.

We successfully applied our new method to derive the 3-D displacement fields associated with one seismic event and for two 24 h periods. The results show that the regular upward dome growth at Mount St. Helens was occasionally offset by coseismic downward displacements of the order of a meter, which significantly affected the calculated daily velocities.

Our 3-D approach also reveals the internal dome structures activated during the events. The existence, location, and distribution of structural discontinuities such as the ones found in this study are of high relevance for numerical and experimental modeling, as they strongly influence the stress distribution within the

dome and potentially lead to local destabilization and disintegration of the spine. Deformation monitoring at volcanic domes is therefore a tool for the localization of potentially unstable areas and for understanding mechanisms of dome growth, deformation, and destabilization.

Acknowledgments

This is a contribution to VOLCAPSE, a research project funded by the European Research Council under the European Union's H2020 Programme/ERC consolidator grant ERC-CoG 646858. J.S. is grateful to the German Academic Exchange Service (DAAD) for providing funding for visiting CVO in July 2014 and to Angie Diefenbach (USGS) for her support during this visit. The camera images were provided by the USGS Cascades Volcano Observatory (CVO). The Seismic data were provided by the University of Washington Pacific Northwest Seismic Network and CVO. Any use of trade, firm, or product names is for descriptive purposes only and does not imply endorsement by the U.S. Government. Figures 8–10c, and 12 were created using GMT [Wessel *et al.*, 2013]. The authors wish to thank Daniel Dzurisin and Michael Clyne (USGS) as well as Ben Kennedy and an anonymous referee for diligently reviewing this manuscript.

References

- Anderson, K., M. Lisowski, and P. Segall (2010), Cyclic ground tilt associated with the 2004–2008 eruption of Mount St. Helens, *J. Geophys. Res.*, *115*, B11201, doi:10.1029/2009JB007102.
- Beauducel, F., M. A. Nandaka, F. Cornet, and M. Diament (2006), Mechanical discontinuities monitoring at Merapi volcano using kinematic GPS, *J. Volcanol. Geotherm. Res.*, *150*(1), 300–312.
- Cashman, K. V., C. R. Thornber, and J. S. Pallister (2008), From dome to dust: Shallow crystallization and fragmentation of conduit magma during the 2004–2006 dome extrusion of Mount St. Helens, Washington, in *A Volcano Rekindled: The Renewed Eruption of Mount St. Helens, 2004–2006*, U.S. Geol. Surv. Prof. Pap. 1750, edited by D. R. Sherrod, W. E. Scott, and P. H. Stauffer, pp. 387–413, U.S. Geol. Surv., Reston, Va.
- Chouet, B. A., and R. S. Matoza (2013), A multi-decadal view of seismic methods for detecting precursors of magma movement and eruption, *J. Volcanol. Geotherm. Res.*, *252*, 108–175.
- de Vries, B. V. W., N. Kerle, and D. Petley (2000), Sector collapse forming at Casita volcano, Nicaragua, *Geology*, *28*(2), 167–170.
- Diefenbach, A. K., J. G. Crider, S. P. Schilling, and D. Dzurisin (2012), Rapid, low-cost photogrammetry to monitor volcanic eruptions: An example from Mount St. Helens, Washington, USA, *Bull. Volcanol.*, *74*(2), 579–587.
- Donnadieu, F., and O. Merle (1998), Experiments on the indentation process during cryptodome intrusions: New insights into Mount St. Helens deformation, *Geology*, *26*(1), 79–82.
- Dzurisin, D., S. C. Moran, M. Lisowski, S. P. Schilling, K. R. Anderson, and C. Werner (2015), The 2004–2008 dome-building eruption at Mount St. Helens, Washington: Epilogue, *Bull. Volcanol.*, *77*(10), 1–17, doi:10.1007/s00445-015-0973-4.
- Gaunt, H. E., P. R. Sammonds, P. G. Meredith, R. Smith, and J. S. Pallister (2014), Pathways for degassing during the lava dome eruption of Mount St. Helens 2004–2008, *Geology*, *42*(11), 947–950.
- Hale, A., E. Calder, G. Wadge, S. Loughlin, and G. Ryan (2009), Modelling the lava dome extruded at Soufrière Hills Volcano, Montserrat, August 2005–May 2006: Part I: Dome shape and internal structure, *J. Volcanol. Geotherm. Res.*, *187*(1–2), 53–68, doi:10.1016/j.jvolgeores.2009.08.023.
- Hale, A. J., and G. Wadge (2008), The transition from endogenous to exogenous growth of lava domes with the development of shear bands, *J. Volcanol. Geotherm. Res.*, *171*(3), 237–257.
- Hibert, C., et al. (2014), Automated identification, location, and volume estimation of rockfalls at Piton de la Fournaise volcano, *J. Geophys. Res. Earth Surf.*, *119*, 1082–1105, doi:10.1002/2013JF002970.
- Holland, A. P., I. M. Watson, J. C. Phillips, L. Caricchi, and M. P. Dalton (2011), Degassing processes during lava dome growth: Insights from Santiaguito lava dome, Guatemala, *J. Volcanol. Geotherm. Res.*, *202*(1–2), 153–166, doi:10.1016/j.jvolgeores.2011.02.004.
- Horton, S. P., R. D. Norris, and S. Moran (2008), Broadband characteristics of earthquakes recorded during a dome-building eruption at Mount St. Helens, Washington, between October 2004 and May 2005, in *A Volcano Rekindled: The Renewed Eruption of Mount St. Helens, 2004–2006*, U.S. Geol. Surv. Prof. Pap. 1750, edited by D. R. Sherrod, W. E. Scott, and P. H. Stauffer, pp. 97–110, U.S. Geol. Surv., Reston, Va.
- Husain, T., D. Elsworth, B. Voight, G. Mattioli, and P. Jansma (2014), Influence of extrusion rate and magma rheology on the growth of lava domes: Insights from particle-dynamics modeling, *J. Volcanol. Geotherm. Res.*, *285*, 100–117.
- Ichihara, M., J. J. Lyons, and A. Yokoo (2013), Switching from seismic to seismo-acoustic harmonic tremor at a transition of eruptive activity during the Shinmoe-dake 2011 eruption, *Earth Planets Space*, *65*(6), 633–643, doi:10.5047/eps.2013.05.003.
- Iverson, R. M., et al. (2006), Dynamics of seismogenic volcanic extrusion at Mount St Helens in 2004–05, *Nature*, *444*(7118), 439–443.
- James, M., S. Robson, H. Pinkerton, and M. Ball (2006), Oblique photogrammetry with visible and thermal images of active lava flows, *Bull. Volcanol.*, *69*(1), 105–108.
- James, M. R., and N. Varley (2012), Identification of structural controls in an active lava dome with high resolution DEMs: Volcán de Colima, Mexico, *Geophys. Res. Lett.*, *39*, L22303, doi:10.1029/2012GL054245.
- James, M. R., H. Pinkerton, and S. Robson (2007), Image-based measurement of flux variation in distal regions of active lava flows, *Geochem. Geophys. Geosyst.*, *8*, Q03006, doi:10.1029/2006GC001448.
- James, M. R., P. How, and P. M. Wynn (2016), Pointcatcher software: Analysis of glacial time-lapse photography and integration with multitemporal digital elevation models, *J. Glaciol.*, *62*(231), 159–169, doi:10.1017/jog.2016.27.
- Johnson, J. B., J. M. Lees, A. Gerst, D. Sahagian, and N. Varley (2008), Long-period earthquakes and co-eruptive dome inflation seen with particle image velocimetry, *Nature*, *456*(7220), 377–381.
- Johnson, J. B., J. J. Lyons, B. J. Andrews, and J. M. Lees (2014), Explosive dome eruptions modulated by periodic gas-driven inflation, *Geophys. Res. Lett.*, *41*, 6689–6697, doi:10.1002/2014GL061310.
- Kendrick, J., Y. Lavallée, T. Hirose, G. Di Toro, A. Hornby, S. De Angelis, and D. Dingwell (2014), Volcanic drumbeat seismicity caused by stick-slip motion and magmatic frictional melting, *Nat. Geosci.*, *7*(6), 438–442.
- Kendrick, J. E., Y. Lavallée, A. Ferk, D. Perugini, R. Leonhardt, and D. B. Dingwell (2012), Extreme frictional processes in the volcanic conduit of Mount St. Helens (USA) during the 2004–2008 eruption, *J. Struct. Geol.*, *38*, 61–76.
- Kennedy, B. M., et al. (2016), Surface tension driven processes densify and retain permeability in magma and lava, *Earth Planet. Sci. Lett.*, *433*, 116–124, doi:10.1016/j.epsl.2015.10.031.
- Major, J. J., C. G. Kingsbury, M. P. Poland, and R. G. Lahusen (2008), Extrusion rate of the Mount St. Helens lava dome estimated from terrestrial imagery, November 2004–December 2005, in *A Volcano Rekindled: The Renewed Eruption of Mount St. Helens, 2004–2006*, U.S. Geol. Surv. Prof. Pap. 1750, edited by D. R. Sherrod, W. E. Scott, and P. H. Stauffer, pp. 237–255, U.S. Geol. Surv., Reston, Va.
- Major, J. J., D. Dzurisin, S. P. Schilling, and M. P. Poland (2009), Monitoring lava-dome growth during the 2004–2008 Mount St. Helens, Washington, eruption using oblique terrestrial photography, *Earth Planet. Sci. Lett.*, *286*(1–2), 243–254.
- Mastin, L. G., M. Lisowski, E. Roeloffs, and N. Beeler (2009), Improved constraints on the estimated size and volatile content of the Mount St. Helens magma system from the 2004–2008 history of dome growth and deformation, *Geophys. Res. Lett.*, *36*, L20304, doi:10.1029/2009GL039863.
- Matoza, R. S., and B. A. Chouet (2010), Subevents of long-period seismicity: Implications for hydrothermal dynamics during the 2004–2008 eruption of Mount St. Helens, *Jo. Geophys. Res.*, *115*, B12206, doi:10.1029/2010JB007839.
- Matoza, R. S., M. A. Garcés, B. A. Chouet, L. D'Auria, M. A. H. Hedlin, and G. P. Waite (2009), The source of infrasound associated with long-period events at Mount St. Helens, *J. Geophys. Res.*, *114*, B04305, doi:10.1029/2008JB006128.

- Matoza, R. S., B. A. Chouet, P. B. Dawson, P. M. Shearer, M. M. Haney, G. P. Waite, S. C. Moran, and T. D. Mikesell (2015), Source mechanism of small long-period events at Mount St. Helens in July 2005 using template matching, phase-weighted stacking, and full-waveform inversion, *J. Geophys. Res. Solid Earth*, *120*, 6351–6364, doi:10.1002/2015JB012279.
- Matthews, S. J., M. C. Gardeweg, and R. S. J. Sparks (1997), The 1984 to 1996 cyclic activity of Lascar Volcano, Northern Chile: Cycles of dome growth, dome subsidence, degassing and explosive eruptions, *Bull. Volcanol.*, *59*(1), 72–82.
- Messerich, J. A., S. P. Schilling, and R. A. Thompson (2008), Digital elevation models of the pre-eruption 2000 crater and 2004–07 dome-building eruption at Mount St. Helens, Washington, USA, *U.S. Geol. Surv. Open File Rep. 2008-1169*, p. 2, U.S. Dept. of the Inter., U.S. Geol. Surv., Reston, Va.
- Moran, S., R. Matoza, M. Garces, M. Hedlin, D. Bowers, W. Scott, D. Sherrod, and J. Vallance (2008a), Seismic and acoustic recordings of an unusually large rockfall at Mount St. Helens, Washington, *Geophys. Res. Lett.*, *35*, L19302, doi:10.1029/2008GL035176.
- Moran, S. C., S. D. Malone, A. I. Qamar, W. A. Thelen, A. K. Wright, and J. Caplan-Auerbach (2008b), Seismicity associated with renewed dome building at Mount St. Helens, 2004–2005, in *A Volcano Rekindled: The Renewed Eruption of Mount St. Helens, 2004–2006*, *U.S. Geol. Surv. Prof. Pap. 1750*, edited by D. R. Sherrod, W. E. Scott, and P. H. Stauffer, pp. 27–60, U.S. Geol. Surv., Reston, Va.
- Neuberg, J., R. Luckett, B. Baptie, and K. Olsen (2000), Models of tremor and low-frequency earthquake swarms on Montserrat, *J. Volcanol. Geotherm. Res.*, *101*(1–2), 83–104, doi:10.1016/S0377-0273(00)00169-4.
- Pallister, J. S., C. R. Thornber, K. V. Cashman, M. A. Clynne, H. A. Lowers, C. W. Mandeville, I. K. Brownfield, and G. P. Meeker (2008), Petrology of the 2004–2006 Mount St. Helens lava dome—Implications for magmatic plumbing and eruption triggering, in *A Volcano Rekindled: The Renewed Eruption of Mount St. Helens, 2004–2006*, *U.S. Geol. Surv. Prof. Pap. 1750*, edited by D. R. Sherrod, W. E. Scott, and P. H. Stauffer, pp. 647–702, U.S. Geol. Surv., Reston, Va.
- Pallister, J. S., K. V. Cashman, J. T. Hagstrum, N. M. Beeler, S. C. Moran, and R. P. Denlinger (2013), Faulting within the Mount St. Helens conduit and implications for volcanic earthquakes, *Geol. Soc. Am. Bull.*, *125*(3–4), 359–376.
- Pan, B., K. Qian, H. Xie, and A. Asundi (2009), Two-dimensional digital image correlation for in-plane displacement and strain measurement: A review, *Meas. Sci. Technol.*, *20*(6), 062001.
- Poland, M., D. Dzuris, R. LaHusen, J. Major, D. Lapcewich, E. Endo, D. Gooding, S. Schilling, and C. Janda (2008), Remote camera observations of lava dome growth at Mount St. Helens, Washington, October 2004 to February 2006, in *A Volcano Rekindled: The Renewed Eruption of Mount St. Helens, 2004–2006*, *U.S. Geol. Surv. Prof. Pap. 1750*, edited by D. R. Sherrod, W. E. Scott, and P. H. Stauffer, pp. 225–236, U.S. Geol. Surv., Reston, Va.
- Rosenau, R., E. Schwalbe, H.-G. Maas, M. Baessler, and R. Dietrich (2013), Grounding line migration and high-resolution calving dynamics of Jakobshavn Isbrae, West Greenland, *J. Geophys. Res. Earth Surf.*, *118*, 382–395, doi:10.1029/2012JF002515.
- Salzer, J. T., M. Nikkhoo, T. R. Walter, H. Sudhaus, G. Reyes-Davila, M. Breton, and R. Arambula (2014), Satellite radar data reveal short-term pre-explosive displacements and a complex conduit system at Volcán de Colima, Mexico, *Front. Earth Sci.*, *2*, 12, doi:10.3389/feart.2014.00012.
- Sparks, R. S. J. (1997), Causes and consequences of pressurisation in lava dome eruptions, *Earth Planet. Sci. Lett.*, *150*(3), 177–189.
- Thelen, W. A., R. S. Crosson, and K. C. Creager (2008), Absolute and relative locations of earthquakes at Mount St. Helens, Washington, using continuous data: Implications for magmatic processes, in *A Volcano Rekindled: The Renewed Eruption of Mount St. Helens, 2004–2006*, *U.S. Geol. Surv. Prof. Pap. 1750*, edited by D. R. Sherrod, W. E. Scott, and P. H. Stauffer, pp. 71–95, U.S. Geol. Surv., Reston, Va.
- Travelletti, J., C. Delacourt, P. Allemand, J. P. Malet, J. Schmittbuhl, R. Toussaint, and M. Bastard (2012), Correlation of multi-temporal ground-based optical images for landslide monitoring: Application, potential and limitations, *ISPRS J. Photogramm. Remote Sens.*, *70*, 39–55.
- Vallance, J. W., D. J. Schneider, and S. P. Schilling (2008), Growth of the 2004–2006 lava-dome complex at Mount St. Helens, Washington, in *A Volcano Rekindled: The Renewed Eruption of Mount St. Helens, 2004–2006*, *U.S. Geol. Surv. Prof. Pap. 1750*, edited by D. R. Sherrod, W. E. Scott, and P. H. Stauffer, pp. 169–208, U.S. Geol. Surv., Reston, Va.
- Voight, B. (2000), Structural stability of andesite volcanoes and lava domes, *Philos. Trans. R. Soc. A*, *358*(1770), 1663–1703.
- Voight, B., et al. (1999), Magma flow instability and cyclic activity at Soufriere Hills Volcano, Montserrat, British West Indies, *Science*, *283*(5405), 1138–1142, doi:10.1126/science.283.5405.1138.
- Waite, G. P., B. A. Chouet, and P. B. Dawson (2008), Eruption dynamics at Mount St. Helens imaged from broadband seismic waveforms: Interaction of the shallow magmatic and hydrothermal systems, *J. Geophys. Res.*, *113*, B02305, doi:10.1029/2007JB005259.
- Walter, T. R. (2011), Low cost volcano deformation monitoring: Optical strain measurement and application to Mount St. Helens data, *Geophys. J. Int.*, *186*(2), 699–705.
- Walter, T. R., D. Legrand, H. D. Granados, G. Reyes, and R. Arambula (2013a), Volcanic eruption monitoring by thermal image correlation: Pixel offsets show episodic dome growth of the Colima volcano, *J. Geophys. Res. Solid Earth*, *118*, 1408–1419, doi:10.1002/jgrb.50066.
- Walter, T. R., A. Ratdomopurbo, Subandriyo, N. Aisyah, K. S. Brotopuspito, J. Salzer, and B. Lühr (2013b), Dome growth and coulée spreading controlled by surface morphology, as determined by pixel offsets in photographs of the 2006 Merapi eruption, *J. Volcanol. Geotherm. Res.*, *261*, 121–129.
- Wessel, P., W. H. F. Smith, R. Scharroo, J. Luis, and F. Wobbe (2013), Generic mapping tools: Improved version released, *Eos Trans. AGU*, *94*(45), 409–410.
- Westerweel, J. (1994), Efficient detection of spurious vectors in particle image velocimetry data, *Exp. Fluids*, *16*(3), 236–247, doi:10.1007/BF00206543.